

The extended range phase shift method for broadband surface wave dispersion measurement from ambient noise and its application in ore deposit characterization

Bao Deng¹, Junlun Li¹, Jiangshan Liu², Changming Shen², Junliu Suwen³, and Qi-Fu Chen³

ABSTRACT

Surface wave tomography using seismic ambient noise has been applied widely in subsurface characterization, the depth of which ranges from a few meters in urban underground engineering to tens of kilometers in delineation of crustal heterogeneities. Currently, multichannel analysis of surface waves with active and passive sources together with some similar techniques has been widely applied to obtain fine near-surface structures. However, it is still difficult to retrieve accurate dispersion curves at low frequencies with those methods to constrain structures at greater depths. To better retrieve surface wave dispersion data at lower frequencies using ambient noise data acquired by dense linear arrays, we use the extended range phase shift (ERPS) method, which can extract broadband dispersions from the ambient noise crosscorrelation functions (CFs). A broadband dispersion curve is obtained by merging a dispersion

curve of medium-to-high frequencies with a dispersion curve of low-to-medium frequencies measured using receivers with different combinations, whereas both curves reflect the local property of the subsurface structure under a subarray with a relatively small aperture. Thus, the horizontal resolution of the inverted models is not compromised, whereas the inverted depth is improved considerably. We first perform a synthetic test to validate the ERPS method, and then apply the method in characterizing the Woxi polymetallic deposit in Hunan, China, where eight 10 km linear arrays using 467 seismic nodes were deployed to record ambient noise. The dispersion data within 0.5–10 Hz are extracted from the CFs using ERPS and then used to invert for the V_S models down to at least 2 km. The inverted structures are found to be consistent with the previous geologic studies and known structures from underground mining, and the proposed passive-source imaging method is considered to be economical and practical for ore deposit explorations.

INTRODUCTION

Ambient noise tomography (ANT) is now widely used to study the subsurface structure as an efficient, cost effective, and environmentally friendly approach compared with conventional seismic reflection imaging using dynamite sources, especially when the investigated areas are too large or the structures of interest are too deep (Shapiro and Campillo, 2004; Yao et al., 2006, 2010; Lin et al., 2008), or in areas where it is difficult to carry out active source surveys (Okada and Suto, 2003; Nakata et al., 2011; Cheng et al., 2016). Aki (1957) first

proposes the spatial autocorrelation (SPAC) method to study the subsurface structure using microtremors and proves the feasibility of extracting Green's function (GF) from seismic ambient noise. In the early 2000s, surface wave empirical GFs between pairs of stations has been estimated by cross-correlating the seismic noise records (Lobkis and Weaver, 2001; Weaver and Lobkis, 2004; Weaver, 2005). In addition, theoretical studies (e.g., Roux et al., 2005) and practical applications also have been carried out (Shapiro and Campillo, 2004; Shapiro et al., 2005). Subsequently, Bensen et al. (2007) systematically summarize the data processing procedure for retrieving

Manuscript received by the Editor 14 May 2021; revised manuscript received 16 December 2021; published ahead of production 15 March 2022; published online 26 April 2022.

¹University of Science and Technology of China, School of Earth and Space Sciences, Hefei, China, University of Science and Technology of China, Mengcheng National Geophysical Observatory, Hefei, China, and University of Science and Technology of China, Institute of Advanced Technology, Center for Advanced Geophysical Sensing and Intelligent Exploration, Hefei, China. E-mail: dbao@mail.ustc.edu.cn; lijunlun@ustc.edu.cn (corresponding author).

²Research Institute of Hunan Provincial Nonferrous Metals Geological Exploration Bureau, Changsha, China. E-mail: 297458114@qq.com; 79067155@qq.com.

³Chinese Academy of Sciences, Institute of Geology and Geophysics, Key Laboratory of Earth and Planetary Physics, Beijing, China. E-mail: suwenjunliu18@mails.ucas.ac.cn; chenqf@mail.igcas.ac.cn.

© 2022 Society of Exploration Geophysicists. All rights reserved.

the GF between a pair of stations from ambient noise, which further promoted the extensive applications of ANT.

As for geotechnical engineering, active-source surface wave surveys initially have been used widely. For near-surface characterization with densely deployed stations, the array-based methods such as the τ - p transform (McMechan and Yedlin, 1981), the frequency-wavenumber transform (Yilmaz, 1987), the phase shift method (Park et al., 1998), or the high-resolution linear Radon transformation (Luo et al., 2008) are often applied to extract dispersion curves. The multichannel analysis of surface waves (MASWs) proposed by Park et al. (1999) is probably one of the most recognized methods for surface wave tomography with linear arrays, which were initially used for high-resolution surface wave characterization with active sources (Miller et al., 1999; Park et al., 2005). Although active MASW performs well in estimating the phase velocity in the medium-to-high frequency range (approximately 10 Hz and above), the phase velocity at lower frequencies estimated by MASW usually bears large uncertainty and, thus, the effectively constrained depth by this method is shallower than 30 m in general (Park et al., 2007). Increasing the depth of investigation by several tens of meters requires an order-of-magnitude increase in the active-source energy or using a multisource offset technique (Park and Shawver, 2009). Thus, the more economical and viable solution is to take advantage of the surface waves derived from seismic ambient noise with lower frequencies (Park et al., 2004, 2007; Luo et al., 2018; Behm et al., 2019). Those aforementioned methods for processing active-source surface waves also have been adopted and used in ANT, often with trivial modifications. For instance, the passive MASW (Park et al., 2004) based on a 2D cross layout and the roadside passive MASW (Park and Miller, 2006) for linear arrays are derived from active MASW. As passive surface waves are used to characterize the subsurface structure, the investigated depth is further increased to a few hundred meters (Park et al., 2007). Subsequently, Cheng et al. (2015) propose the bidirectional shot mode by sorting common virtual source gathers to replace the traditional roll-along mode of the MASW, which improves the efficiency of data acquisition. Their method treats each receiver as a virtual source and sorts the cross-correlation functions (CFs) between the receivers to construct common virtual source gathers. A linear array is divided into a series of subarrays, for each of which the dispersion curve is measured using stations within the subarray. The local dispersion curves are then used to invert for the 1D stratified V_S models under each subarray, and a pseudo 2D V_S profile is obtained by constructing the local 1D stratified models together. Because a linear array cannot unambiguously determine the directionality of the noise sources in the offline direction (Garofalo et al., 2016; Foti et al., 2018), the determined phase velocities might be systematically biased. Cheng et al. (2016) propose the multichannel analysis of passive surface waves (MAPS) method to further improve the estimation accuracy of the dispersion curves by compensating for the noise directionality. Wu et al. (2017) propose the cross-correlation and phase-shifting (CCPS) method, which can further improve the signal-to-noise ratio (S/N) of the dispersion images for surface waves.

Although the aforementioned studies on surface wave ANT have had many successful applications in the past two decades, it is still rather difficult to extract broadband dispersion curves from a few seconds to several Hz or even higher without severely compromising the horizontal resolution or reliability of the inverted model. More specifically, the aperture of the subarray needs to be increased to derive

dispersion data at lower frequencies, but too large an aperture may violate the assumption of layered medium for the phase shift and other similar methods (Aki, 1957; Park et al., 1999), and sometimes the lowest frequency which can be retrieved using passive MASW may not be extended even with an increased subarray aperture. Thus, it is not easy to obtain a subsurface tomogram with high resolution in the near surface and with adequate constraint at greater depths because a broadband dispersion curve is rather difficult to obtain using passive MASW or other conventional passive methods.

In this study, we propose a novel extended range phase shift (ERPS) method to extract stable broadband dispersion curves which only reflect the local velocity structure under a subarray with a relatively small aperture. A broadband dispersion curve is obtained by merging a dispersion curve of medium-to-high frequencies with a dispersion curve of low-to-medium frequencies measured using receivers with different combinations. Tomography using those broadband dispersion curves reflects variation in the local structures and has relatively high resolution in the horizontal and vertical directions. In the following, we first introduce the theory and procedure of ERPS, followed by a synthetic test to demonstrate the merits of ERPS compared with the conventional passive MASW. Finally, the method is applied to characterize a polymetallic deposit using surface wave ANT, where eight 10 km dedicated linear arrays with 467 seismic nodes were deployed to record ambient noise.

METHOD

In the conventional phase shift method, it is assumed that the sources are distant from the receivers and the surface wave can be approximated as plane waves propagating in a stratified medium. The dispersion image can be calculated by (Wu et al., 2017)

$$V(f, C_T) = \sum_{i=1}^N \sum_{j=i+1}^N \exp\left(-i \frac{2\pi f(x_j - x_i)}{C_R(f)}\right) \exp\left(i \frac{2\pi f(x_j - x_i)}{C_T}\right), \quad (1)$$

where $V(f, C_T)$ denotes the value of the dispersion image at a particular frequency f and a scanning phase velocity C_T ; $C_R(f)$ denotes the average real phase velocity under the station array at frequency f ; x_i and x_j are the coordinates for the pair of the stations i and j , respectively; N is the total number of stations in the linear array for deriving the dispersion image; and the exponential term $\exp(-i((2\pi f(x_j - x_i))/C_R(f)))$ reflects the observed phase shift when the surface wave propagates from station i to station j , which can be directly calculated in the frequency domain (Park et al., 1999). For a particular frequency f , $V(f, C_T)$ is maximized when the scanning phase velocity C_T equals the real phase velocity $C_R(f)$. Consequently, the maximal values in the dispersion image can be used to estimate the frequency-dependent phase velocity $C_R(f)$ of the subsurface structure. More generally, equation 1 can be modified to the following form:

$$V(f, C_T) = \sum_{i=1}^N \sum_{j=i+1}^N \exp\left(-i 2\pi f \int_{x_i}^{x_j} S_R(x) dx\right) \exp\left(i 2\pi f \int_{x_i}^{x_j} S_T(x) dx\right), \quad (2)$$

where $S_R(x) = 1/C_R(x)$ denotes the real slowness at position x and $S_T(x) = 1/C_T(x)$ denotes the scanning slowness along the propagation path. However, a tradeoff exists between the lowest extracted frequency and the horizontal resolution of the inverted subsurface structure when using the phase shift method: more receivers in a larger subarray are required to estimate the dispersion curve at lower frequencies, i.e., the obtained phase velocity reflects the average velocity over a larger area. To solve this issue, we propose the ERPS method to retrieve broadband dispersion curves without compromising the horizontal resolution (Figure 1). ERPS essentially has two components: the internal-array phase shift (IPS) and the external-array phase shift (EPS). The IPS component retrieves a dispersion curve of medium-to-high frequencies from the dispersion image calculated from the phase shift among the receivers within a subarray similar to passive MASW for ambient noise. In comparison, the EPS component first calculates individual dispersion images from the phase shift between a certain receiver external to a subarray and all the receivers within the subarray, and then retrieves a dispersion curve of low-to-medium frequencies with improved quality and stability from the stacked dispersion image. We will show in the following sections that the dispersion curve from EPS only reflects the subsurface structure under the same subarray of IPS evaluation and is independent of the structures between the external receiver and the subarray. To obtain a desired broadband dispersion curve, the dispersion curves retrieved by IPS and EPS for the same subarray are then merged by weighted stacking. The details of ERPS are elaborated on next.

Internal-array phase shift

A subarray in ERPS is defined by the station index n at its center (blue triangle in Figure 1) and the subarray aperture $r = md$, where m is the number of stations from the center to the edge of the subarray, and d is the interstation distance (Figure 1). The stations within the subarray are referred to as the internal stations (black), and the stations outside are referred to as the external stations (gray). In ERPS, the IPS component for calculating the medium-to-high frequency dispersion curve is similar to CCPS in Wu et al. (2017), which only uses CFs from the stations within a subarray to calculate the dispersion image $V_{\text{int}}(f, C_T)$ corresponding to the subsurface structures:

$$V_{\text{int}}(f, C_T) = \sum_{k=n-m}^{n+m} \sum_{l=k+1}^{n+m} C_{kl} \exp\left(i2\pi f \frac{x_{kl}}{C_T}\right), \quad (3)$$

where C_{kl} represents the observed phase shift between station k and station l and x_{kl} is the corresponding distance. Depending on whether the causal, acausal, or the symmetric part of the CF is used (Cheng et al., 2016), the corresponding phase shift C_{kl}^+ (positive time), C_{kl}^- (negative time), or $(C_{kl}^+ + C_{kl}^-)/2$ is selected for C_{kl} . Although IPS performs well in extracting dispersion curves in the medium-to-high frequency range, it is not suitable for extracting low-frequency dispersions. This is because the aperture r of the subarray is not large enough to discriminate the phase variation of long-wavelength surface waves; thus, the dispersion image $V_{\text{int}}(f, C_T)$ does not have a distinct energy peak at lower frequencies. Alternatively, an artificial energy peak may appear at an incorrect velocity for the lower frequencies (Park et al., 1999).

External-array phase shift

To invert for structures at greater depths, the dispersion curves at lower frequencies need to be extracted, which is the aim of the proposed EPS component in ERPS. Compared with the IPS component, which only uses the internal stations, the data recorded by external stations also contribute to the calculation of the dispersion data in the EPS component. The external stations are treated as virtual sources, and the internal stations of the subarray are regarded as receivers. The dispersion image $V_{\text{ext}}^k(f, C_T)$ derived with the k th external virtual source and all the receivers from a subarray is

$$V_{\text{ext}}^k(f, C_T) = \sum_{l=n-m}^{n+m} \exp\left(-i2\pi f \int_{x_k}^{x_l} S_R(x) dx\right) \exp\left(i2\pi f \int_{x_k}^{x_l} S_T(x) dx\right). \quad (4)$$

The propagation path from the k th external virtual source to the l th receiver within the subarray can be further divided into two segments, i.e., the external and the internal paths separated by the edge of the subarray:

$$V_{\text{ext}}^k(f, C_T) = \sum_{l=n-m}^{n+m} \left\{ \exp\left(-i2\pi f \int_{x_k}^{x_{n+m}} S_R(x) dx\right) \exp\left(-i2\pi f \int_{x_{n+m}}^{x_l} S_R(x) dx\right) \right\} \\ \left\{ \exp\left(i2\pi f \int_{x_k}^{x_{n+m}} S_T(x) dx\right) \exp\left(i2\pi f \int_{x_{n+m}}^{x_l} S_T(x) dx\right) \right\}, \quad (5)$$

where the integration from x_k to x_{n+m} accounts for the external phase shift from the receiver k to the edge of the subarray, and the integration from x_{n+m} to x_l accounts for the internal phase shift within the subarray. It is obvious that the external paths for all receivers within the subarray centered at x_n to receiver k are independent of the summation and can be pulled out. Thus, equation 5 can be rewritten as

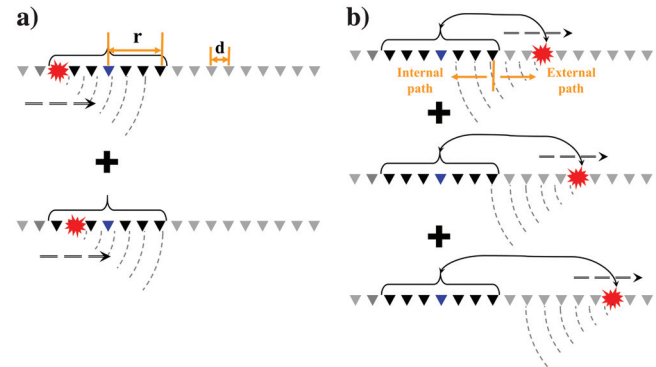


Figure 1. The schematic illustration of the proposed ERPS method. (a) The IPS and (b) the EPS. The inverted triangles denote the stations, which are divided into three different categories: the center station (blue) that defines the position for the current subarray, the internal stations (black) within the subarray, and the external stations (gray) outside the subarray. The red stars represent the virtual sources in the calculation.

$$V_{\text{ext}}^k(f, C_T) = \left\{ \exp\left(-i2\pi f \int_{x_k}^{x_{n+m}} S_R(x) dx\right) \exp\left(i2\pi f \int_{x_k}^{x_{n+m}} S_T(x) dx\right) \right\} \\ \sum_{l=n-m}^{n+m} \exp\left(-i2\pi f \int_{x_{n+m}}^{x_l} S_R(x) dx\right) \exp\left(i2\pi f \int_{x_{n+m}}^{x_l} S_T(x) dx\right), \quad (6)$$

where the remaining exponential terms in the summation represent the phase shift within the subarray. Taking the same assumption of a stratified medium under the subarray as in IPS, equation 6 can be simplified as

$$V_{\text{ext}}^k(f, C_T) = \left\{ \exp\left(-i2\pi f \int_{x_k}^{x_{n+m}} S_R(x) dx\right) \exp\left(i2\pi f \int_{x_k}^{x_{n+m}} S_T(x) dx\right) \right\} \\ \sum_{l=n-m}^{n+m} \exp\left(-i2\pi f \frac{x_{n+m,l}}{C_R(f)}\right) \exp\left(i2\pi f \frac{x_{n+m,l}}{C_T}\right), \quad (7)$$

where $x_{n+m,l}$ denotes the distance between the $(n+m)$ th and l th receivers. For the EPS component, the contribution of the external path on the dispersion image can be easily removed by taking the absolute value:

$$|V_{\text{ext}}^k(f, C_T)| = \left| \sum_{l=n-m}^{n+m} \exp\left(-i2\pi f \frac{x_{n+m,l}}{C_R}\right) \exp\left(i2\pi f \frac{x_{n+m,l}}{C_T}\right) \right|, \quad (8)$$

because the absolute value of the terms in the curly bracket is a unit. Thus, the common external path does not contribute to the amplitude $|V_{\text{ext}}^k(f, C_T)|$ of the dispersion image, and the estimated

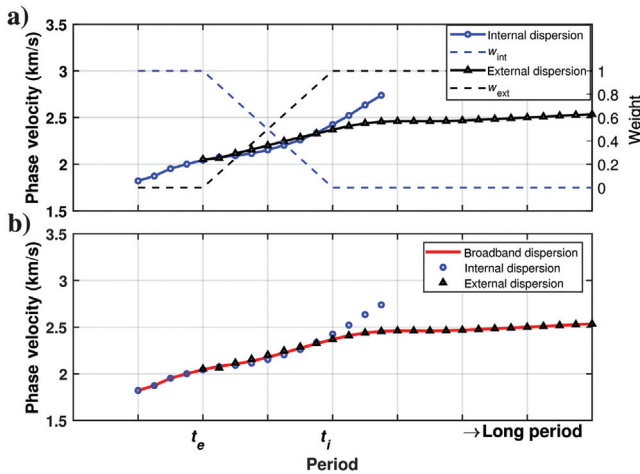


Figure 2. An illustration for the merging of the internal and external dispersion curves. (a) Dispersion curves before merging. The solid blue and black lines represent the internal and external dispersion curves, respectively. The dashed blue and black lines represent the corresponding merging weights for the respective dispersion curves. (b) The red line denotes the broadband dispersion curve after merging.

phase velocity C_R only reflects the structure under the receivers within the subarray. In practice, the phase shift C_{kl} between the external station k and the internal station l is used, and we take absolute values on both sides of equation 4:

$$|V_{\text{ext}}^k(f, C_T)| = \left| \sum_{l=n-m}^{n+m} C_{kl} \exp\left(i2\pi f \frac{x_{kl}}{C_T}\right) \right|, \quad (9)$$

which is equivalent to equation 8. More importantly, because $|V_{\text{ext}}^k(f, C_T)|$ is independent of the external path and thus independent of the choice of a virtual source, the dispersion images from different external virtual sources can be stacked:

$$V_{\text{ext}}(f, C_T) = \sum_{\substack{k=1 \\ k \notin [n-m, n+m]}}^N |V_{\text{ext}}^k(C_T, f)| \\ = \sum_{k=1}^N \left| \sum_{l=n-m}^{n+m} C_{kl} \exp\left(i2\pi f \frac{x_{kl}}{C_T}\right) \right|, \\ k \notin [n-m, n+m] \quad (10)$$

which further stabilizes the dispersion image and improves the S/N, especially at the lower frequencies with weak energy. It should be noted that in EPS the external paths from a virtual source to all receivers within a subarray are assumed to be identical, which is reasonable for low-frequency surface waves with large wavelengths and less affected by structural heterogeneities. However, the propagation paths of surface waves with higher frequencies are more affected by the ragged free-surface subsurface heterogeneities and thus are less consistent. As a result, the dispersion images at higher frequencies may not be improved notably through the stacking of additional external virtual sources.

Merging the dispersion curves

The IPS component of ERPS is almost equivalent to the conventional passive MASW approach based on the phase shift method, and the additional information extracted in ERPS is indeed provided by the EPS component. Thus, merging the dispersion curves provided by the IPS and EPS components in ERPS is crucial for taking advantage of the internal- and external-array phase shifts. At appropriate overlapped periods where the dispersion curves from IPS and EPS are similar, different weights for the internal and external dispersion curves are applied to construct a broadband dispersion curve which can be used to characterize structures from shallow to deep (Figure 2). That is, a broadband dispersion curve $C(t)$ is obtained by

$$C(t) = w_{\text{int}}(t)C_{\text{int}}(t) + w_{\text{ext}}(t)C_{\text{ext}}(t), \quad (11)$$

where $C_{\text{int}}(t)$ and $C_{\text{ext}}(t)$ are the internal and external dispersion curves at a particular period t , respectively, and $w_{\text{int}}(t)$ and $w_{\text{ext}}(t)$ are the corresponding period-dependent weighting factors (Figure 2a) which sum to one for all periods. We empirically determine the longest reliable period t_i for the internal dispersion

curve (blue line) and the shortest reliable period t_e for the external dispersion curve (black line) based on the consistency between the internal and external dispersion curves and the corresponding noise level in the dispersion images. The weighting factor $w_{\text{int}}(t)$ varies linearly from 1.0 to 0 as the period goes from t_e to t_i , and vice versa for $w_{\text{ext}}(t)$. For periods shorter than t_e , the merged dispersion curve is identical to the internal dispersion curve, whereas it is identical to the external dispersion curve for periods longer than t_i . Thus, not only can the merged dispersion curve be used to resolve the shallow structure with high resolution, but also it can be used to constrain the deeper structure in the inversion reliably.

Inversion for the 2D V_S profile

By extracting and merging the internal and external dispersion curves for subarrays centered at different stations, we obtain a series of broadband dispersion curves reflecting adjacent local structures along a linear array. All of the local dispersion curves are inverted simultaneously to obtain a 2D profile with horizontal and vertical constraints (Hayashi, 2008), which improves the inversion stability. The nonlinear inverse problem can be expressed as

$$D = G(M), \quad (12)$$

where D is the broadband phase dispersion curves along a linear array extracted by ERPS, M is the true 2D V_S model, and G is the sensitivity kernel. The inverse problem is linearized by first-order Taylor expansion:

$$D \approx G(\hat{M}) + J\delta M, \quad (13)$$

where \hat{M} is the current model, δM represents the difference between the true model and the current model, and J is the Jacobian matrix, which is evaluated via numerical perturbations (e.g., Xia et al., 1999). The data residual δD between the observed and theoretical dispersion curves is related to the model difference δM by

$$\delta D = D - G(\hat{M}) \approx J\delta M. \quad (14)$$

To stabilize the inversion, equation 14 can be solved iteratively with smoothness constraints (e.g., Nakata et al., 2019), and the corresponding objective function is

$$\Phi(\delta M) = \|\delta D - J\delta M\|_2^2 + \lambda_v \|L_v(\delta M)\|_2^2 + \lambda_h \|L_h(\delta M)\|_2^2, \quad (15)$$

where L_v and L_h are the second-order Tikhonov regularization to constrain the model variation in the vertical and horizontal directions, respectively, with λ_v and λ_h being the corresponding weighting terms. The model update is then obtained by

$$\delta \hat{M} = (J^T J + \lambda_v L_v^T L_v + \lambda_h L_h^T L_h)^{-1} J^T \delta D, \quad (16)$$

and the model can be updated iteratively by

$$M_{j+1} = M_j + \delta \hat{M}, \quad (17)$$

where M_j and M_{j+1} are the inverted model at the j th and $(j+1)$ th iterations, respectively.

SYNTHETIC TEST

We first design a 2D synthetic test to verify the effectiveness of the ERPS method in extracting broadband dispersion curves. We use random sources to generate many individual wavefields, the summation of which simulate the seismic ambient noise. The CFs between pairs of receivers in the linear array are then calculated. The elastic model used in the 2D synthetic test is shown in Figure 3a, and no attenuation is assumed in the simulation. The P-wave velocity and density are converted from the S-wave velocity using the empirical relationships given by Brocher (2005). There are 50 geophones deployed between 25 and 35 km with a 200 m interval. A total of 500 active sources are randomly distributed on the surface at both sides of the receiver array. Ricker wavelets are used for the sources, with the central frequencies for different sources randomly varying between 0.5 and 8 Hz, and the amplitudes randomly varying between 0.1 and 1. The finite-difference method (Virieux, 1986; Levander, 1988) is used to generate the full elastic wavefield, with $\Delta x = \Delta z = 12.5$ m and $\Delta t = 1$ ms. Because the actual contribution to the reconstruction of the surface wave GFs from seismic ambient noise originates from the stationary phase zones close to the inline direction and the contributions from the offline directions should cancel out (Nakata et al., 2019), the 2D numerical experiment along the inline direction should suffice for

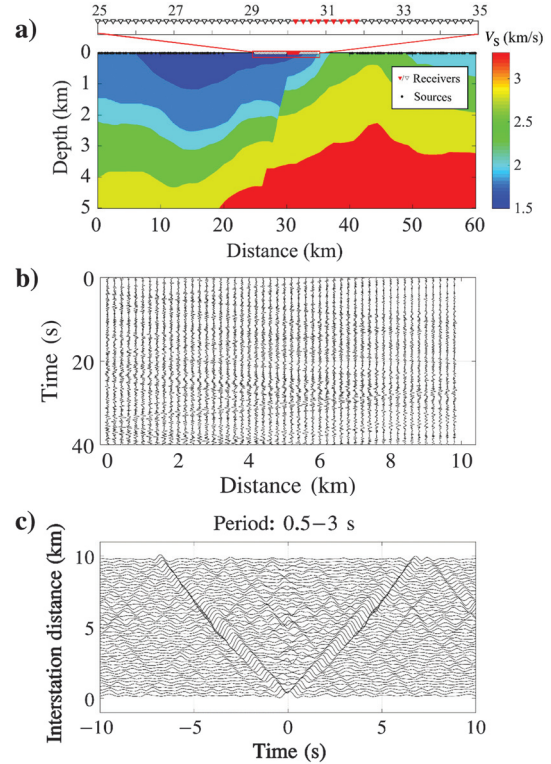


Figure 3. The heterogeneous velocity model and data generated in the synthetic test. (a) The V_S model, the black dots represent the explosion sources, inverted triangles represent all the receivers, and the red triangles represent a subarray for the subsequent analysis. (b) The synthetic records generated by the finite-difference method with superposed Gaussian noise. (c) The CFs of the synthetic records between the first and the remaining receivers. The stations in the subarray marked by red are used to calculate the dispersion image in Figure 4.

validating the method. Gaussian noise with amplitude of 5% of the maximum amplitude of the surface waves is added. The total wavefields from all of the random sources are shown in Figure 3b. The corresponding CFs are shown in Figure 3c, in which the horizontal axis indicates the time delay for the CF between a pair of stations, and the interstation distance is shown in the vertical axis. Hayashi et al. (2021) recently also synthesize 3D stochastic wave propagation for ambient noise using the 3D finite-difference method.

To compare the dispersion images calculated by IPS, which is almost equivalent to the conventional passive MASW and EPS, we select nine stations in the middle of the linear array (red inverted triangles) to construct a subarray with an aperture of 0.8 km for the evaluation, and the remaining stations in the linear array are treated as the virtual sources for EPS. The respective dispersion images using IPS and EPS are shown in Figure 4. To better illustrate the peak energy at different frequencies, it should be noted that the energy at each frequency is normalized independently (Park et al., 2004; Cheng et al., 2015). The extracted dispersion curves (blue lines) based on the peak value at each frequency in the dispersion images and the theoretical dispersion curves (red lines) calculated using the local stratified medium under the subarray (Thomson, 1950; Haskell, 1953; Kennett, 1974; Herrmann, 2013) are plotted together in the subfigures. For IPS, the dispersion curve is rather close to the theoretical one down to approximately 1 Hz. Below 1 Hz, the dispersion image peaks become distorted, and the extracted dispersion curve starts to deviate from the theoretical value. In comparison, the dispersion image from EPS has distinct peaks at the correct velocities down to approximately 0.5 Hz (2 s), and the extracted dispersion curve still matches well with the theoretical one at much lower frequencies. In this case, the lowest frequency retrieved by EPS is about one-half that by IPS, i.e., the depth of the inverted model using EPS can be at least doubled compared with the depth inverted by IPS alone. In addition, the consistency between the extracted dispersion curve using EPS and the theoretical one in Figure 4b clearly shows that the external heterogeneous structures do not affect the calculation of the dispersion image for a subarray.

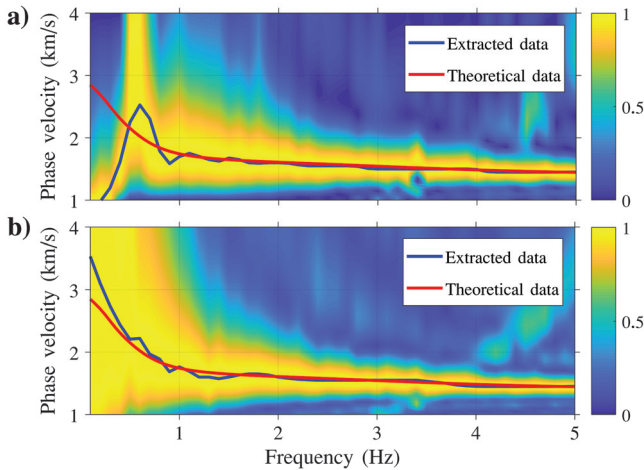


Figure 4. The comparison of dispersion images using IPS and EPS. (a) The dispersion image calculated by IPS and (b) the dispersion image calculated by EPS. The red line in each subfigure represents the theoretical dispersion curve, whereas the blue lines are the dispersion curves extracted using (a) IPS and (b) EPS, respectively.

Furthermore, we compare the models obtained using IPS and ERPS in Figure 5. Based on the comparisons with the true model, it is found that the effectively inverted depth from IPS is shallower than 0.8 km, whereas the effectively inverted depth from ERPS is approximately 2 km. Therefore, ERPS significantly improves the investigation depth compared with IPS while retaining the resolution for the shallower sections.

APPLICATION TO REAL DATA

In the following, we further apply the ERPS method to extract broadband dispersion curves for ANT in the Woxi Au-Sb-W deposit, western Hunan Province, China. The strong topographic relief and complex surface conditions including dense vegetation render it prohibitive for an active-source seismic reflection imaging with a reasonable budget, and a passive seismic survey is thus a viable alternative for the subsurface characterization. In September and October 2019, we deployed eight dense linear arrays to collect the ambient noise data for about one month. Each linear array is approximately 10 km in length, with 467 SmartSolo 3C 5 Hz nodes in total (Figure 6a). The interstation spacing varies from 100 to 400 m. More specifically, the spacing is 200 m for L160, 400 m for L360, and 250 m for the remaining six lines, whereas the spacing is further reduced to 100 m within the 4 km in the central sections of the linear arrays, where the target zone is approximately situated. The crossline spacing is approximately 500 m for all eight lines. Recent studies have demonstrated that the Rayleigh wave at lower frequencies

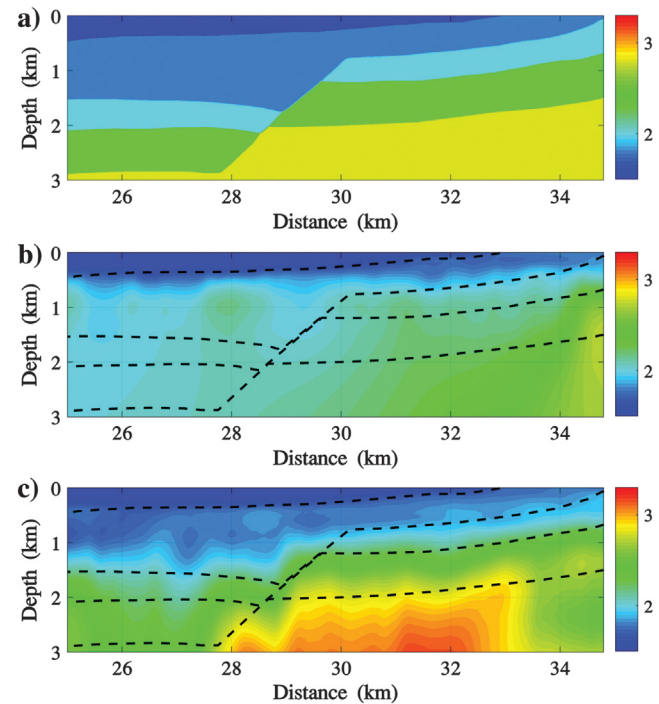


Figure 5. Comparison of the true model and the inverted models using the dispersion data from IPS and ERPS in the synthetic test. (a) The true V_S model. (b) The inverted V_S model using the dispersion data from IPS. (c) The inverted V_S model using the dispersion data from ERPS. The dashed black lines in (b) and (c) denote the boundaries of the strata as shown in (a). Note the quality of the inverted model at greater depths close to the two edges becomes slightly worse due to limited aperture.

also can be retrieved from long-term ambient noise records acquired by the short-period nodes (Lin et al., 2013; Wang et al., 2019). Similarly, we calculate the CFs of ambient noise following the practice of Bensen et al. (2007). The raw noise records are first downsampled to 50 Hz from 250 Hz with an antialiasing filter. Then, the continuous records are cut into 1 h long segments for preprocessing, including mean and trend removal, spectral whitening in the frequency domain, temporal normalization in the time domain, and band-pass filtering between 0.1 and 5 s before the CFs are calculated. The final CFs of L160 obtained by stacking the CFs calculated with hourly noise records are shown in Figure 6b. The CFs of high S/N are directional, indicating an inhomogeneous distribution of noise sources. Thus, it is crucial to take the directionality of the noise source into consideration when extracting the dispersion curves. Because a linear array cannot unambiguously determine the directionality of the noise sources in the offline direction (Garofalo et al., 2016; Foti et al., 2018), the determined phase velocities might be systematically biased (Asten and Hayashi, 2018; Asten et al., 2019). That is, the measured phase velocities using the linear array may be higher than the actual values due to nonomnidirectional source distributions, resulting in a surface wave GF propagating in the offline direction (Foti et al., 2018). Thus, for the following discussions we will not be focused on interpreting the absolute values of the inverted structures. Instead, the velocity contrast and heterogeneities of the subsurface structures will be analyzed in detail. In this survey, the CFs in the causal part correspond to signals propagating from southeast to northwest. Thus, the CFs in the causal part are attributed to noise sources in the southeastern direction, and those in the acausal part are attributed to noise sources in the opposite direction. To extract dispersion curves from CFs constructed from inhomogeneously distributed noise sources, we calculate each of the internal and external dispersion images (equations 3 and 10) three times using the causal, acausal, and the symmetric parts of CFs, respectively, and then compare their overall S/N and the continuities of the energy peaks in the dispersion images.

The dispersion images from IPS and EPS using an aperture of 1400 m are shown in Figure 7. For IPS, the calculated dispersion image using the causal part of the CFs has high S/N between 1.5 and 8 Hz (Figure 7a), whereas the S/N of the acausal part is much worse and incoherent (Figure 7b). The symmetric stacking of CFs (Figure 7c) is similar to the causal part because the amplitude of the CFs in the acausal part is actually much lower than that in the causal part (Figure 6). For EPS, the dispersion image using the causal part of CFs has high S/N between 0.5 and 6 Hz (Figure 7d), whereas the acausal part of CFs also is much worse in comparison (Figure 7e). The symmetric stacking of the CFs also is worse than the causal part at low frequencies (Figure 7f) due to the detrimental contribution from the acausal part in this case. Therefore, it should be noted in the dispersion data processing that the CFs with high S/N may only exist in one part of CFs, and the symmetric stacking involving the other part may actually compromise the quality of the dispersion images (Bensen et al., 2007; Cheng et al., 2015).

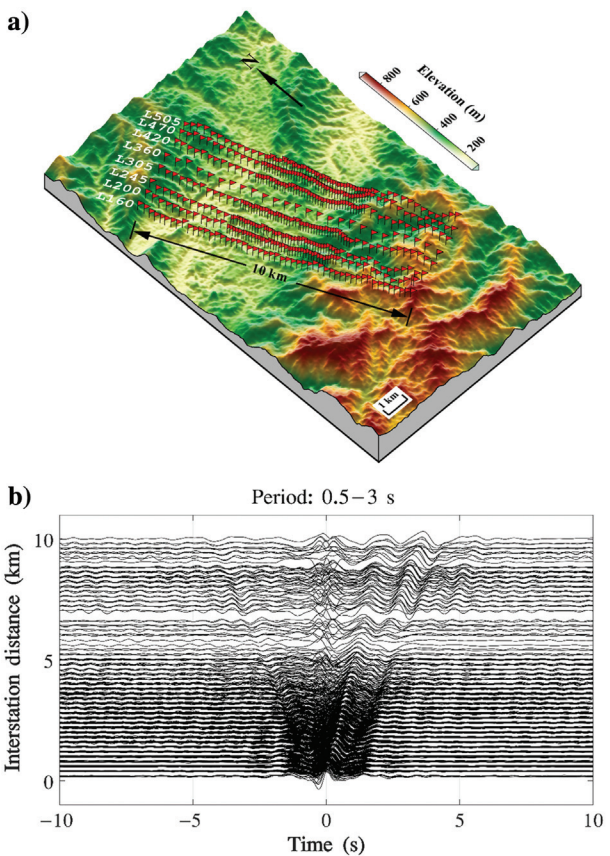


Figure 6. The dense linear arrays deployed in the Woxi deposit and the CFs for L160 as an example. (a) Eight dense linear arrays, namely, L160, L200, L245, L305, L360, L420, L470, and L505, are deployed from west to east with roughly equal crossline spacing. (b) The CFs filtered between 0.5 and 3 s from L160.

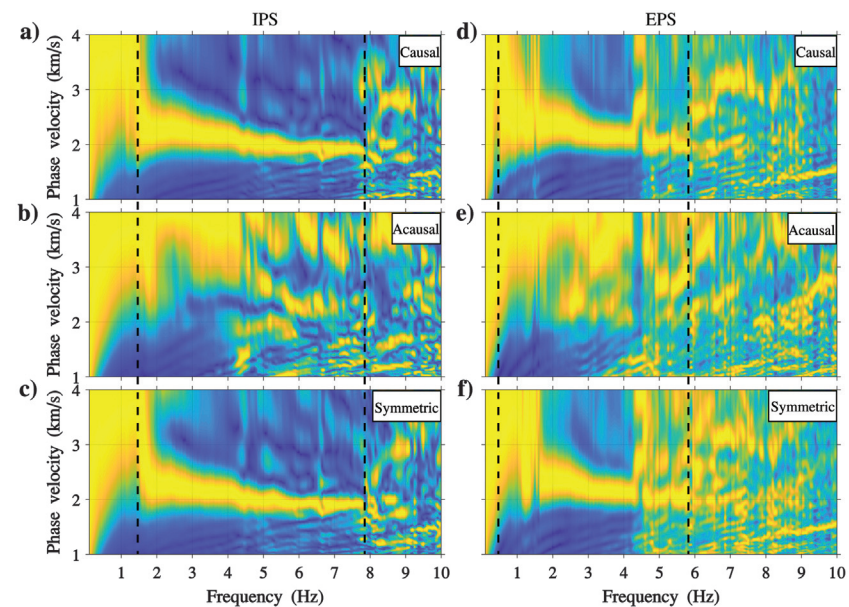


Figure 7. Comparison of the dispersion images using IPS and EPS. (a) The causal and (b) acausal parts of CFs and (c) the symmetric stacking of the CFs calculated by IPS. (d–f) The same as (a)–(c), respectively, except they are calculated by EPS. In each subfigure, the energy is normalized independently at each frequency for the best visual illustration.

In this case, the lowest frequency of the extracted dispersion curve from the dispersion image using IPS is approximately 1.5 Hz (approximately 0.7 s) (Figure 7a), whereas it is approximately 0.5 Hz (2 s) from the dispersion image using EPS (Figure 7d), which can at least triple the maximum inverted depth compared with that by IPS. Still, the energy peaks in the dispersion image using EPS at frequencies greater than 6 Hz are less coherent compared with those using IPS. Hence, using IPS to derive dispersions curves at medium-to-high frequencies, and using EPS to derive dispersion curves at lower-to-medium frequencies, ERPS can yield reliable broadband dispersion curves by properly merging those within different frequency ranges.

In processing the real data, to reflect the local structure and to improve the horizontal resolution of the shallow subsurface, the aperture is further reduced to 600 m when calculating the dispersion image for IPS, whereas it is still 1400 m for EPS. Considering the noise levels and the continuities of the energy peaks, we typically pick the external dispersion curves between 0.5 and 5 Hz and pick the internal dispersion curves between 2 and 10 Hz. The dispersion curves from the internal array using IPS (cyan lines) and those from the external array using EPS (gray lines) for L160 are shown in Figure 8a. The horizontal axis is scaled in the frequency above 1 Hz and in the period below 1 Hz to fully stretch the broadband dispersion curves and expose more details. The dispersion curves from IPS and EPS match reasonably well at approximately 3 Hz, whereas the internal dispersion curves (cyan) trend upward too rapidly below 2.5 Hz (0.4 s). In addition, most of the dispersion curves from EPS can extend up to approximately 5 Hz (0.2 s), whereas those from IPS can extend up to approximately 10 Hz. Thus, by merging the dispersion curves obtained from IPS and EPS between 5 and 2.5 Hz (0.2–0.4 s) as indicated by the dashed lines (Figure 8a), we obtain the broadband dispersion curves shown in Figure 8b.

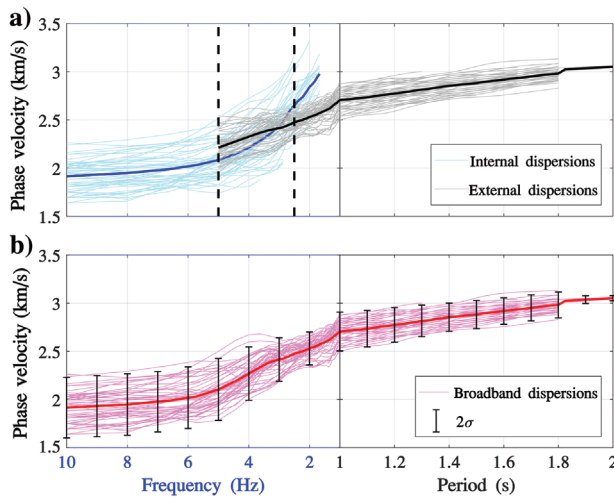


Figure 8. The dispersion curves for the subarrays of L160 extracted by ERPS. (a) The internal dispersion curves (cyan) and the external dispersion curves (gray) before merging. The overlapped frequencies for merging are from 5 to 2.5 Hz (0.2–0.4 s) as shown between the two dashed black lines. (b) Broadband dispersion curves (magenta) after the weighted merging (equation 11) of the respective dispersion curves extracted by IPS and EPS. The bold blue, black, and red lines indicate the average of the individual internal, external, and broadband dispersion curves, respectively.

With the extracted dispersion curves, a V_S profile can be obtained using equations 16 and 17. For each linear array, an average dispersion curve is first calculated from all dispersion curves of this array. An initial layered S-wave velocity model \hat{M} is constructed from the average dispersion curve using the empirical relationship in Xia et al. (1999), and the regularization weights λ_v and λ_h , whose typical values range from 0.1 to 1, are provided empirically. The initial 1D S-wave velocity model for L160 is shown in Figure 9a as an example, and the sensitivity kernels indicate that the Rayleigh wave phase velocities in the periods of 0.1–2 s are most sensitive to the S-wave velocity in the upper 2.5 km (Figure 9b). Nevertheless, structures just below 2.5 km in depth can still be constrained with some uncertainty.

It takes several iterations (equation 17) to obtain the final velocity model for each linear array, and a typical convergence curve is shown in Figure 10. An inverted 2D velocity model reflects the velocity variation relative to the free surface, and to facilitate subsequent geologic interpretations, we apply local pseudosurface-relief corrections by shifting the inverted model in the vertical direction according to the surface elevation along a linear array. The final results for the eight dense linear arrays are shown in Figure 11. Although all of the 2D V_S profiles are obtained separately, they show general consistency with gradual change from L160 to L505 or from southwest to northeast. The inverted V_S model for L360 where the receivers are deployed more sparsely is relatively smooth in comparison because the horizontal resolution of the model is reduced due to the increased interstation spacing. Although reversed velocity layers may generate higher mode surface waves in general, the higher modes should be absent in this particular survey. This is likely because the reversed velocity structures are relatively deep and the velocity contrast is minor. Then, a 3D regional V_S velocity model also can be obtained by interpolating the eight 2D models spatially through cubic splines, and a horizontal slice of the 3D model at 0 km elevation is shown in Figure 12. It is obvious that the velocity shows a distinct dichotomous feature

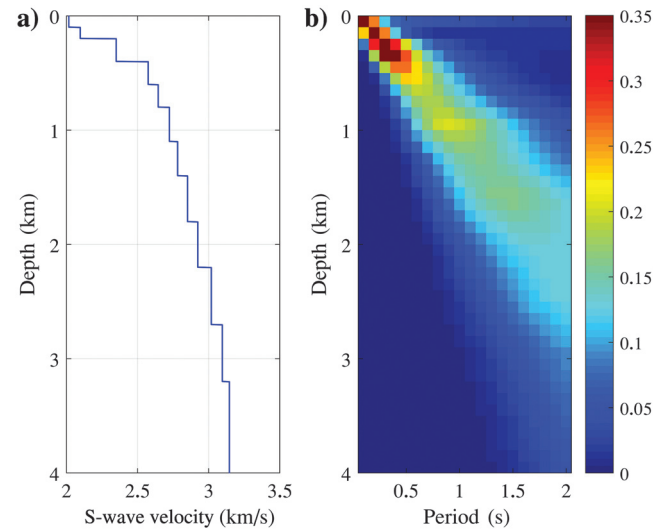


Figure 9. (a) The initial 1D S-wave model for L160 and (b) the amplitudes of the phase-velocity sensitivity kernels at different periods. The sensitivity kernels indicate that the Rayleigh wave phase velocities in the periods of 0.1–2 s are most sensitive to the S-wave velocity in the upper 2.5 km.

separated by the Woxi F_1 fault, with the structures in the southeast being slower in general than their counterparts in the northwest.

To further validate our inversion result, L160 is selected for a detailed geologic interpretation, below which underground mining has been taking place. The surface outcrops, known gold veins, vertical exploration wells, and extended faults are overlaid with the inverted V_S profile shown in Figure 13. The solid bold red lines represent the extensions of the known surface fault traces (F_1

and F_{15}), and the dashed bold red lines represent the inferred faults. A sharp S-wave velocity contrast is present across the major Woxi F_1 fault, which dips between 25° and 45° to the north by northwest direction (Wang et al., 2000; Kuang et al., 2004) and extends over 2 km in depth (Gu et al., 2007). Although the surface traces of the inferred F_2 and F_9 faults can be identified, their dipping angles are

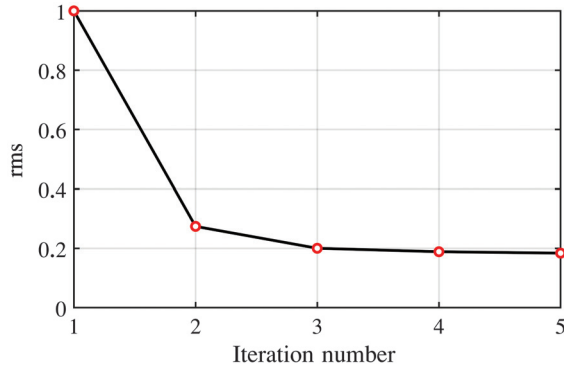


Figure 10. A typical convergence curve with iteration for the surface wave ANT using the broadband dispersion curve extracted by ERPS. This plot shows the variation of the relative rms error of the dispersion data with iteration for L160.

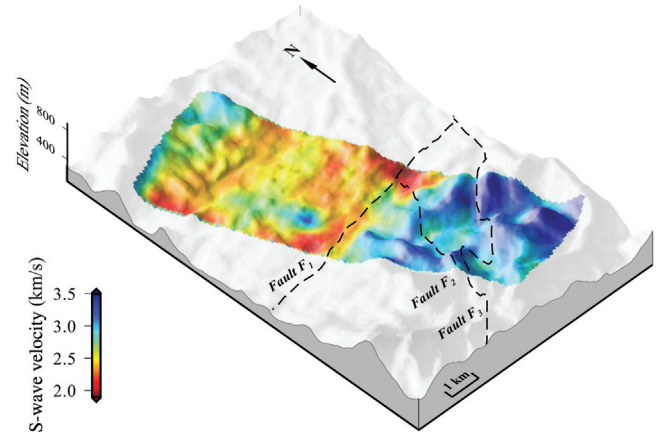


Figure 12. A horizontal slice of the 3D model interpolated from the eight 2D profiles at the zero elevation. The dashed black lines indicate the projection of the faults F_1 , F_2 , and F_3 .

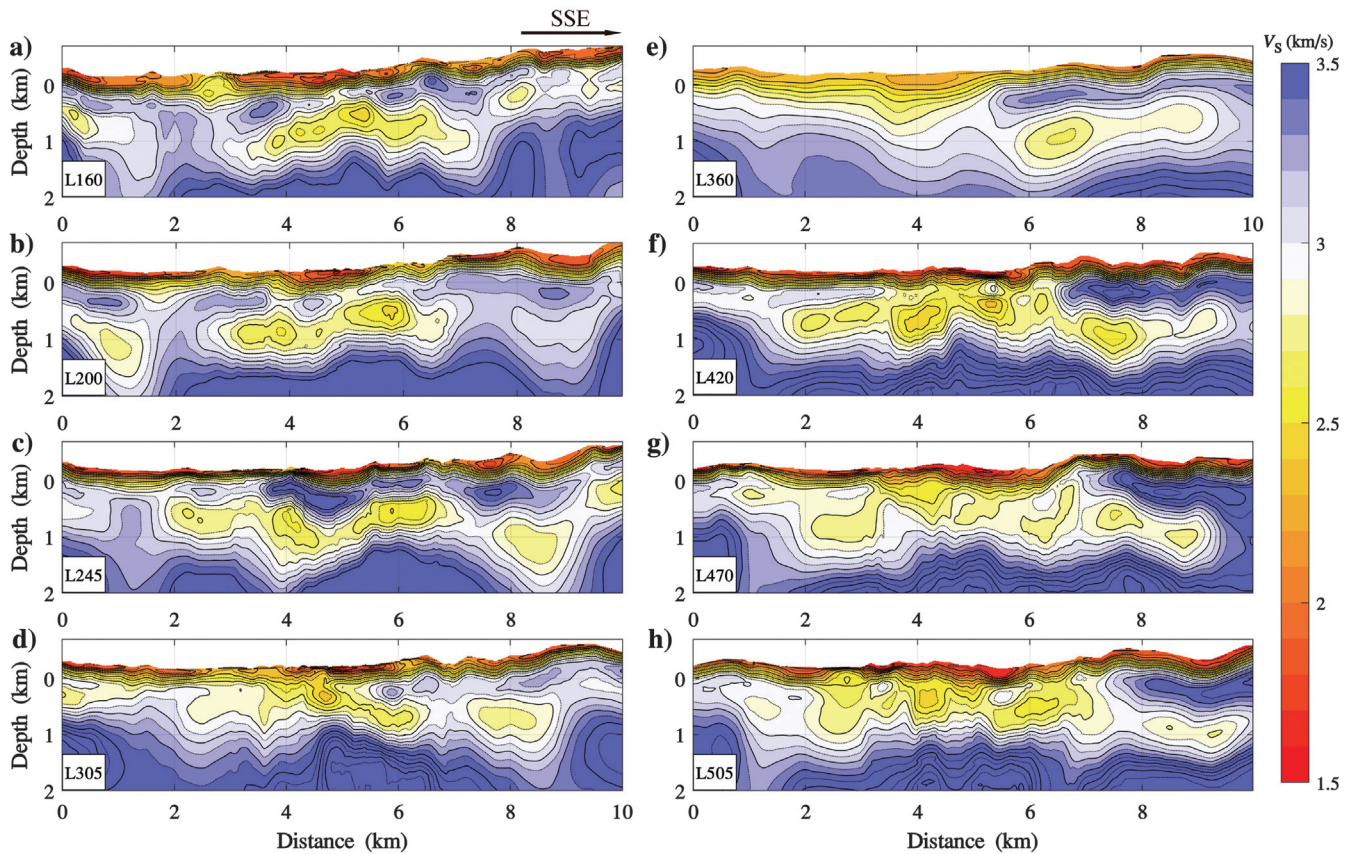


Figure 11. The inverted V_S profiles for the eight lines. The line numbers are shown in the white boxes at the lower-left corner in each subplot. The depth is referenced to the mean sea level.

not clear from the surface evidence. Thus, the dashed lines represent the inferred extensions based on the velocity contrast in the inverted velocity model. Because there is no sonic logging in the study area, the exact S-wave velocity is not directly available for comparison. Instead, the exploration wells (ZK1 and ZK001 in Figure 13) provide rock samples and delineations of the strata boundaries (solid dark green lines). The lithology along well ZK001 can be divided into four major formations, i.e., the argillaceous slates (Fm. I),

sandy calcareous slates (Fm. II), argillaceous slates (Fm. III), and sandy calcareous slates (Fm. IX) in sequence. In general, the argillaceous slates are mechanically weaker than the sandy calcareous slates, and, thus, the S-wave velocities in Fm. I and Fm. III are lower than their counterparts in Fm. II and Fm. IX. Importantly, the positions and elevation changes of the subsurface tunnels (solid yellow lines) along the veins (V7 and V8) also match well with the velocity contrast in the model. Because the metallogenic mechanism is likely of the metamorphic-hydrothermal type controlled by strata in the Woxi deposit (Zhu and Peng, 2015), we speculate that the gold vein may extend further along the upper and lower boundaries of the low-velocity body as shown by the dashed yellow lines. Although there is no further data or information available to corroborate our speculation currently, the inferred gold veins can be selected as the primary targets for future prospecting.

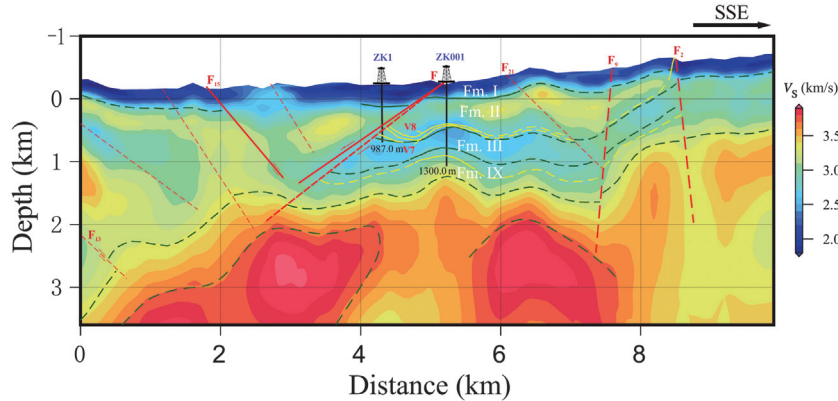


Figure 13. Geologic interpretation for L160. The background image is the inverted V_s profile using the broadband dispersion curves obtained by ERPS. The solid red lines indicate the extension of known faults from the surface traces, and the dashed red lines represent the inferred faults. The black lines indicate the two vertical exploration wells (ZK1 and ZK001), the solid dark green lines are the known boundaries for different strata, the dashed green lines are the inferred boundaries, and the solid yellow lines indicate the tunnels for gold mining, whose locations and variation in elevation correspond well with the velocity structure. The dashed yellow lines are the gold veins inferred from the velocity structure. This figure together with Figure 6a and Figure 12 are plotted with the Generic Mapping Tools (Wessel et al., 2019).

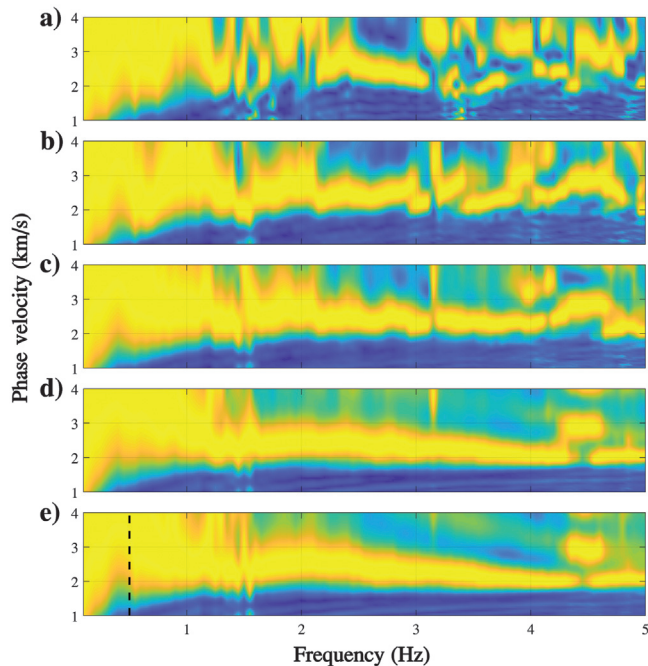


Figure 14. Comparison of the dispersion images for different numbers of external sources in EPS. Using (a) a single external source and (b) 5, (c) 10, (d) 20, and (e) 40 external sources.

DISCUSSION

Although the surface wave energy is dominant in the observed wavefield, other seismic phases irrelevant to dispersion estimation also are present. At higher frequencies, the CFs from station pairs with a short interstation distance are contaminated by body waves (Nakata et al., 2019), which is detrimental for extracting the dispersion curves from CFs. In comparison, the surface waves are dominant in the CFs estimated from station pairs separated by a larger distance because the amplitude of the body waves decays more rapidly ($1/r$) than that of the surface wave ($1/\sqrt{r}$), where r is the interstation distance.

In addition, the influence of the near-field effects gradually diminishes with the increase in interstation distance (Yao et al., 2006). Park et al. (1999) find that the surface waves can be approximated as plane waves (allowing for phase shift estimation) provided that the offset is greater than half the wavelength, and even shorter offset is sometimes viable as well. Thus, the EPS component that uses virtual sources external to a subarray with increased interstation distances can calculate dispersion images with improved stability and S/N at lower frequencies.

Recent studies have made efforts to characterize and remedy the influence of directionality of noise sources, e.g., the MAPS waves proposed by Cheng et al. (2016) and the root mean square (rms)-ratio selection stacking of CFs proposed by Xie et al. (2020). In general, deploying a 2D array with uniform receiver spacing and SPAC-like methods to process the ambient noise can better suppress the influence of the noise-source directionality, which, however, is prohibitive economically for the ore deposits characterization in such a mountainous area covered by dense forests. In the future, the proposed ERPS can take advantage of the preceding methods to further improve the accuracy of the calculated dispersion curves.

In addition, the stacking of the dispersion images from many external individual virtual sources is instrumental in improving the stability and S/N. We show that EPS, in general, has more fold numbers compared with IPS in Appendix A. In addition, Figure 14 compares the quality of the stacked dispersion images for the varying number of external virtual sources in EPS. With a single external source

(Figure 14a), the dispersion image is disrupted at many frequencies and does not exhibit distinct energy peaks at lower frequencies. As the number of external sources increases from 5 to 20 (Figure 14b–14d), the energy peak in the dispersion image becomes increasingly continuous at higher frequencies, and more distinct and converged at lower frequencies as well. When 40 external sources are used (Figure 14e), not only does the energy peak in the dispersion image become continuous at higher frequencies but also it is distinct and converged well below 1 Hz, and a reliable dispersion curve can be extracted at 0.5 Hz and above.

For real data processing, we have summarized two general rules: (1) in general, the internal dispersion images become stable when the aperture is approximately 4–6 times the interstation distance, and the aperture of EPS should range from about twice as large as that of IPS to half of the maximum target depth, and (2) it also is recommended that the total number of receivers in a linear array should be sufficient to allow the construction of several subarrays from the linear array. It also should be noted that if proper surface waves can be acquired through active seismic waves in the study area, the near-surface structures can be better characterized using dispersion curves with higher frequencies.

CONCLUSION

In this study, we propose a new method called ERPS to calculate dispersion images from ambient noise recorded by dense linear arrays. The ERPS method that includes the IPS and the EPS components can effectively improve the S/N and convergence of the energy peaks in the dispersion image at lower frequencies, while retaining the quality of the dispersion image at higher frequencies. Consequently, reliable broadband dispersion curves can be extracted and used to invert subsurface structures. Not only shallow structures can be determined with high resolution, but also structures at greater depth can be well constrained. We first demonstrate the effectiveness of ERPS with a synthetic test, and then apply the method to an ambient noise data set acquired by eight 10 km linear arrays in the Woxi Au-Sb-W deposit, western Hunan, China. Using the broadband dispersion curves, 2D velocity profiles along the linear arrays are inverted, and a 3D regional velocity model also is constructed from the 2D profiles through interpolation. To further validate our inversion results, we also interpret an inverted V_s profile with known geology and mining data. We find the velocity structures match well with known surface geology, faults, and strata characterized by wells, as well as the gold veins under production. Thus, we believe the proposed ERPS method using seismic ambient noise can be used as an economical alternative to active-source seismic reflection imaging for orebody characterization.

ACKNOWLEDGMENTS

The authors are grateful to the associate editor, C. Birnie, and three anonymous reviewers for their very detailed and constructive comments and suggestions which greatly improved our manuscript. The authors also thank Y. Li, J. Gao, and Y. He for their contributions in the field work, and thank J. Xu for his help in preparing Generic Mapping Tools scripts for plotting some of the figures. This study is supported by the National Natural Science Foundation of China (grant no. 41874048) and the National Key Research and Development Projects 2018YFC0603500.

DATA AND MATERIALS AVAILABILITY

Data associated with this research are confidential and cannot be released.

APPENDIX A COMPARISON OF THE FOLD NUMBER IN ERPS

We show in general the fold number of stacking for EPS is larger than that in IPS which is traditionally used to extract dispersion curves for linear arrays. A dense linear array consisting of N stations in total is shown in Figure 1 in the main text, and we consider a general case in which the subarray is situated somewhere in the middle of the linear array but not at the two ends. Assuming there are m stations within aperture r in a subarray, i.e., there are $2m + 1$ internal stations and $N - 2m - 1$ external stations, the fold number of stacking for IPS is then

$$N_{\text{int}} = C_{2m+1}^2 = m(2m + 1). \quad (\text{A-1})$$

In EPS, we use a combination of internal stations and external stations, and the number of stacking is

$$N_{\text{ext}} = C_{N-2m-1}^1 C_{2m+1}^1 = (N - 2m - 1)(2m + 1). \quad (\text{A-2})$$

To compare the numbers of stacking between EPS and IPS, we find the boundary condition $N_{\text{int}} = N_{\text{ext}}$:

$$m(2m + 1) = (N - 2m - 1)(2m + 1). \quad (\text{A-3})$$

We simplify equation A-3 and obtain the following formula:

$$N = 3m + 1. \quad (\text{A-4})$$

That is, when N equals $3m + 1$, the fold numbers of IPS and EPS become equal. In other words, as long as the total number of stations N is greater than $3m + 1$, the fold number of EPS is more than that of IPS, which is easily satisfied in practice where the aperture of the subarray is usually less than one-tenth of the length of the linear array.

REFERENCES

- Aki, K., 1957, Space and time spectra of stationary stochastic waves, with special reference to microtremors: Bulletin of the Earthquake Research Institute, **35**, 415–456.
- Asten, M. W., and K. Hayashi, 2018, Application of the spatial auto-correlation method for shear-wave velocity studies using ambient noise: Surveys in Geophysics, **39**, 633–659, doi: [10.1007/s10712-018-9474-2](https://doi.org/10.1007/s10712-018-9474-2).
- Asten, M. W., A. Yong, S. Foti, K. Hayashi, A. J. Martin, W. J. Stephenson, J. F. Cassidy, and J. Coleman, 2019, A preliminary assessment of uncertainties attributed by analysts, array types and processing algorithms for microtremor observations, via the COSMOS blind trials: ASEG, Extended Abstracts, 1–4.
- Behm, M., F. Cheng, A. Patterson, and G. S. Soreghan, 2019, Passive processing of active nodal seismic data: Estimation of V_p/V_s ratios to characterize structure and hydrology of an alpine valley infill: Solid Earth, **10**, 1337–1354, doi: [10.5194/se-10-1337-2019](https://doi.org/10.5194/se-10-1337-2019).
- Bensen, G. D., M. H. Ritzwoller, M. P. Barmin, A. L. Levshin, F. Lin, M. P. Moschetti, N. M. Shapiro, and Y. Yang, 2007, Processing seismic ambient noise data to obtain reliable broad-band surface wave dispersion measure-

- ments: *Geophysical Journal International*, **169**, 1239–1260, doi: [10.1111/j.1365-246X.2007.03374.x](https://doi.org/10.1111/j.1365-246X.2007.03374.x).
- Brocher, T. M., 2005, Empirical relations between elastic wavespeeds and density in the earth's crust: *Bulletin of the Seismological Society of America*, **95**, 2081–2092, doi: [10.1785/0120050077](https://doi.org/10.1785/0120050077).
- Cheng, F., J. Xia, Y. Luo, Z. Xu, L. Wang, C. Shen, R. Liu, Y. Pan, B. Mi, and Y. Hu, 2016, Multichannel analysis of passive surface waves based on crosscorrelations: *Geophysics*, **81**, no. 5, EN57–EN66, doi: [10.1190/geo2015-0505.1](https://doi.org/10.1190/geo2015-0505.1).
- Cheng, F., J. Xia, Y. Xu, Z. Xu, and Y. Pan, 2015, A new passive seismic method based on seismic interferometry and multichannel analysis of surface waves: *Journal of Applied Geophysics*, **117**, 126–135, doi: [10.1016/j.jappgeo.2015.04.005](https://doi.org/10.1016/j.jappgeo.2015.04.005).
- Foti, S., F. Hollender, F. Garofalo, D. Albarello, M. Asten, P. Y. Bard, C. Comina, C. Cornou, B. Cox, G. Di Giulio, and T. Forbriger, 2018, Guidelines for the good practice of surface wave analysis: A product of the InterPACIFIC project: *Bulletin of Earthquake Engineering*, **16**, 2367–2420, doi: [10.1007/s10518-017-0206-7](https://doi.org/10.1007/s10518-017-0206-7).
- Garofalo, F., S. Foti, F. Hollender, P. Y. Bard, C. Cornou, B. R. Cox, M. Ohrnberger, D. Sicilia, M. Asten, G. Di Giulio, and T. Forbriger, 2016, InterPACIFIC project: Comparison of invasive and non-invasive methods for seismic site characterization. Part I: Intra-comparison of surface wave methods: *Soil Dynamics and Earthquake Engineering*, **82**, 222–240, doi: [10.1016/j.soildyn.2015.12.010](https://doi.org/10.1016/j.soildyn.2015.12.010).
- Gu, X., O. Schulz, F. Vavtar, J. Liu, M. Zheng, and S. Fu, 2007, Rare earth element geochemistry of the Woxi W-Sb-Au deposit, Hunan Province, South China: *Ore Geology Reviews*, **31**, 319–336, doi: [10.1016/j.oregeorev.2005.01.003](https://doi.org/10.1016/j.oregeorev.2005.01.003).
- Haskell, N. A., 1953, The dispersion of surface waves on multilayered media: *Bulletin of the Seismological Society of America*, **43**, 17–34, doi: [10.1785/BSSA0430010017](https://doi.org/10.1785/BSSA0430010017).
- Hayashi, K., 2008, Development of surface-wave methods and its application to site investigations: Ph.D. thesis, Kyoto University.
- Hayashi, K., M. Craig, S. Tan, C. Konishi, H. Suzuki, M. Tahara, K. Falkenstein, and S. Chen, 2021, Common-midpoint spatial autocorrelation analysis of seismic ambient noise obtained from a spatially unaliased sensor distribution: *Geophysics*, **86**, no. 4, EN51–EN62, doi: [10.1190/geo2020-0467.1](https://doi.org/10.1190/geo2020-0467.1).
- Herrmann, R. B., 2013, Computer programs in seismology: An evolving tool for instruction and research: *Seismological Research Letters*, **84**, 1081–1088, doi: [10.1785/0220110096](https://doi.org/10.1785/0220110096).
- Kennett, B. L. N., 1974, Reflections, rays, and reverberations: *Bulletin of the Seismological Society of America*, **64**, 1685–1696, doi: [10.1785/BSSA0640061685](https://doi.org/10.1785/BSSA0640061685).
- Kuang, W., D. Gu, and X. Liu, 2004, Discussion on the mineralization geological features and metallogenetic model of Woxi Au-Sb-W deposit in west Hunan: *Gold Geology*, **25**, 1001–1277.
- Levander, A. R., 1988, Fourth-order finite-difference P-SV seismograms: *Geophysics*, **53**, 1425–1436, doi: [10.1190/1.1442422](https://doi.org/10.1190/1.1442422).
- Lin, F., M. P. Moschetti, and M. H. Ritzwoller, 2008, Surface wave tomography of the western United States from ambient seismic noise: Rayleigh and Love wave phase velocity maps: *Geophysical Journal International*, **173**, 281–298, doi: [10.1111/j.1365-246X.2008.03720.x](https://doi.org/10.1111/j.1365-246X.2008.03720.x).
- Lin, F. C., D. Z. Li, R. W. Clayton, and D. Hollis, 2013, High-resolution 3D shallow crustal structure in Long Beach, California: Application of ambient noise tomography on a dense seismic array: *Geophysics*, **78**, no. 4, Q45–Q56, doi: [10.1190/geo2012-0453.1](https://doi.org/10.1190/geo2012-0453.1).
- Lobkis, O. I., and R. L. Weaver, 2001, On the emergence of the Green's function in the correlations of a diffuse field: *The Journal of the Acoustical Society of America*, **110**, 3011–3017, doi: [10.1121/1.1417528](https://doi.org/10.1121/1.1417528).
- Luo, Y., J. Lin, Y. Yang, L. Wang, X. Yang, and J. Xie, 2018, Joint inversion of active sources and ambient noise for near-surface structures: A case study in the Balikun Basin, China: *Seismological Research Letters*, **89**, 2256–2265, doi: [10.1785/0220180140](https://doi.org/10.1785/0220180140).
- Luo, Y., J. Xia, R. D. Miller, Y. Xu, J. Liu, and Q. Liu, 2008, Rayleigh-wave dispersive energy imaging by high-resolution linear Radon transform: *Pure and Applied Geophysics*, **165**, 903–922, doi: [10.1007/s00024-008-0338-4](https://doi.org/10.1007/s00024-008-0338-4).
- McMechan, G. A., and M. J. Yedlin, 1981, Analysis of dispersive waves by wave field transformation: *Geophysics*, **46**, 869–874, doi: [10.1190/1.1441225](https://doi.org/10.1190/1.1441225).
- Miller, R. D., J. Xia, C. B. Park, J. Ivanov, and E. Williams, 1999, Using MASW to map bedrock in Olathe, Kansas: 69th Annual International Meeting, SEG, Expanded Abstracts, 433–436, doi: [10.1190/1.1821045](https://doi.org/10.1190/1.1821045).
- Nakata, N., L. Guaglietti, and A. Fichtner, 2019, Seismic ambient noise: Cambridge University Press.
- Nakata, N., R. Snieder, T. Tsuji, K. Larner, and T. Matsuoka, 2011, Shear wave imaging from traffic noise using seismic interferometry by cross-coherence: *Geophysics*, **76**, no. 6, SA97–SA106, doi: [10.1190/geo2010-0188.1](https://doi.org/10.1190/geo2010-0188.1).
- Okada, H., and K. Suto, 2003, The microtremor survey method: SEG.
- Park, C. B., and R. D. Miller, 2006, Roadside passive MASW: 19th EGGS Symposium on the Application of Geophysics to Engineering and Environmental Problems, cp-181.
- Park, C. B., R. D. Miller, and J. Xia, 1998, Imaging dispersion curves of surface waves on multi-channel record: 68th Annual International Meeting, SEG, Expanded Abstracts, 1377–1380, doi: [10.1190/1.1820161](https://doi.org/10.1190/1.1820161).
- Park, C. B., R. D. Miller, and J. Xia, 1999, Multichannel analysis of surface waves: *Geophysics*, **64**, 800–808, doi: [10.1190/1.1444590](https://doi.org/10.1190/1.1444590).
- Park, C. B., R. D. Miller, J. Xia, and J. Ivanov, 2004, Imaging dispersion curves of passive surface waves: 74th Annual International Meeting, SEG, Expanded Abstracts, 1357–1360, doi: [10.1190/1.1851112](https://doi.org/10.1190/1.1851112).
- Park, C. B., R. D. Miller, J. Xia, and J. Ivanov, 2007, Multichannel analysis of surface waves (MASW) — Active and passive methods: *The Leading Edge*, **26**, 60–64, doi: [10.1190/1.2431832](https://doi.org/10.1190/1.2431832).
- Park, C. B., R. D. Miller, J. Xia, J. Ivanov, G. V. Sonnichsen, J. A. Hunter, R. L. Good, R. A. Burns, and H. Christian, 2005, Underwater MASW to evaluate stiffness of water-bottom sediments: *The Leading Edge*, **24**, 724–728, doi: [10.1190/1.1993267](https://doi.org/10.1190/1.1993267).
- Park, C. B., and J. B. Shawver, 2009, MASW survey using multiple source offsets: 22nd EGGS Symposium on the Application of Geophysics to Engineering and Environmental Problems, Extended Abstracts, 639–649.
- Roux, P., K. G. Sabra, W. A. Kuperman, and A. Roux, 2005, Ambient noise cross correlation in free space: Theoretical approach: *Journal of the Acoustical Society of America*, **117**, 79–84, doi: [10.1121/1.1830673](https://doi.org/10.1121/1.1830673).
- Shapiro, N. M., and M. Campillo, 2004, Emergence of broadband Rayleigh waves from correlations of the ambient seismic noise: *Geophysical Research Letters*, **31**, L07614, doi: [10.1029/2004GL019491](https://doi.org/10.1029/2004GL019491).
- Shapiro, N. M., M. Campillo, L. Stehly, and M. H. Ritzwoller, 2005, High-resolution surface-wave tomography from ambient seismic noise: *Science*, **307**, 1615–1618, doi: [10.1126/science.1108339](https://doi.org/10.1126/science.1108339).
- Thomson, W. T., 1950, Transmission of elastic waves through a stratified solid medium: *Journal of Applied Physics*, **21**, 89–93, doi: [10.1063/1.1699629](https://doi.org/10.1063/1.1699629).
- Virieux, J., 1986, P-SV wave propagation in heterogeneous media: Velocity-stress finite-difference method: *Geophysics*, **51**, 889–901, doi: [10.1190/1.1442147](https://doi.org/10.1190/1.1442147).
- Wang, J., E. Peng, M. Lei, and S. Liu, 2000, The formation and evolution of Woxi Fault, Xiangxi Gold Mine, western Hunan: *Journal of Guilin Institute of Technology*, **20**, 0315–0318.
- Wang, Y. D., F. C. Lin, and K. M. Ward, 2019, Ambient noise tomography across the Cascadia subduction zone using dense linear seismic arrays and double beamforming: *Geophysical Journal International*, **217**, 1668–1680, doi: [10.1093/gji/ggaa109](https://doi.org/10.1093/gji/ggaa109).
- Weaver, R., 2005, Diffuse fields in open systems and the emergence of the Green's function: *The Journal of the Acoustical Society of America*, **117**, 2394–2394, doi: [10.1121/1.4809391](https://doi.org/10.1121/1.4809391).
- Weaver, R. L., and O. I. Lobkis, 2004, Diffuse fields in open systems and the emergence of the Green's function (L): *The Journal of the Acoustical Society of America*, **116**, 2731–2734, doi: [10.1121/1.1810232](https://doi.org/10.1121/1.1810232).
- Wessel, P., J. F. Luis, L. Uieda, R. Scharroo, F. Wobbe, W. H. F. Smith, and D. Tian, 2019, The generic mapping tools version 6: *Geochemistry, Geophysics, Geosystems*, **20**, 5556–5564, doi: [10.1029/2019GC008515](https://doi.org/10.1029/2019GC008515).
- Wu, D., C. Sun, and M. Lin, 2017, Active seismic surface wave dispersion imaging method based on cross-correlation and phase-shifting (in Chinese): *Progress in Geophysics*, **32**, 1693–1700.
- Xia, J., R. D. Miller, and C. B. Park, 1999, Estimation of near-surface shear-wave velocity by inversion of Rayleigh waves: *Geophysics*, **64**, 691–700, doi: [10.1190/1.1444578](https://doi.org/10.1190/1.1444578).
- Xie, J., Y. Yang, and Y. Luo, 2020, Improving cross-correlations of ambient noise using an rms-ratio selection stacking method: *Geophysical Journal International*, **222**, 989–1002, doi: [10.1093/gji/ggaa232](https://doi.org/10.1093/gji/ggaa232).
- Yao, H., R. D. van der Hilst, and M. V. de Hoop, 2006, Surface-wave array tomography in SE Tibet from ambient seismic noise and two-station analysis — I. Phase velocity maps: *Geophysical Journal International*, **166**, 732–744, doi: [10.1111/j.1365-246X.2006.03028.x](https://doi.org/10.1111/j.1365-246X.2006.03028.x).
- Yao, H., R. D. van der Hilst, and J. P. Montagner, 2010, Heterogeneity and anisotropy of the lithosphere of SE Tibet from surface wave array tomography: *Journal of Geophysical Research, Solid Earth*, **115**, B12307, doi: [10.1029/2009JB007142](https://doi.org/10.1029/2009JB007142).
- Yilmaz, O., 1987, Seismic data processing: SEG.
- Zhu, Y., and J. Peng, 2015, Infrared microthermometric and noble gas isotope study of fluid inclusions in ore minerals at the Woxi orogenic Au-Sb-W deposit, western Hunan, South China: *Ore Geology Reviews*, **65**, 55–69, doi: [10.1016/j.oregeorev.2014.08.014](https://doi.org/10.1016/j.oregeorev.2014.08.014).

Biographies and photographs of the authors are not available.